One step synthesis of vertically grown Mn-doped ZnO nanorods for photocatalytic application

Nita D. Raskar[1] · Dnyaneshwar V. Dake[1] · Vijay A. Mane[1] · Elias Stathatos[2] · Uday Deshpande[3] · Babasaheb Dole[1]

Abstract

Pure and Mn-doped ZnO nanorods thin films on glass substrates were successfully synthesized by a one-step hydrothermal route. It was confirmed from XRD data that pure and Mn-doped ZnO samples show hexagonal (wurtzite) structures and the particle size was found to be in the range 27–31 nm. From XRD data it was clearly found that vertical growth along (002) plane after Mn-doping into ZnO lattice. Functional groups and chemical species were detected using FT-IR spectra. Diameter and length of ZnO nanorods were determined by TEM which is in the range 350 nm, 1–4 μm respectively. UV–Vis results exhibit red shift with increasing Mn concentration in ZnO lattice. The 5% Mn-doped ZnO sample exhibits higher fluorescence intensity in visible region with surface defects. The electrical resistance of pure and Mn-doped ZnO nanorods was demonstrated by I–V characteristics. It was explicitly outlined from Raman spectra E_2^{high} mode was shifted towards the higher wavenumber from 439 to 440 cm^{-1} owing to Mn doping in ZnO lattice. The average surface area, pore volume, and pore diameter were measured by using the BET isotherm. The photocatalytic activity of pure and Mn-doped ZnO was evaluated by the degradation of methylene blue (MB) under UV–Vis light irradiation which indicates that 5% Mn-doped ZnO nanorods have better photocatalytic activity than other samples.

1 Introduction

In a recent development, ZnO has attracted extensive attention of scientists and technologists owing to its vital properties. Nowadays research on ZnO is hotly debated due to its photocatalytic performance. ZnO is the material having high tunability of charge carriers, carrier mobility, optical transparency and low hazardous to the environment [1]. ZnO is a nontoxic semiconductor with a wide band gap ~ 3.37 eV and it has large exciton binding energy (60 meV) at room temperature [2]. Bulk ZnO has a hexagonal (wurtzite) structure, belongs to the space group ($P6_3mc$) and having unit cell parameters a = b = 3.253 Å and c = 5.209 Å [3]. ZnO has various applications such as LEDs [4], lasers [5], gas sensor [6], UV photodetector [7], solar cell [8] and photocatalytic activity [9], etc. due to its distinctive properties. Most of the researchers have been proved that ZnO can degrade most kinds of persistent organic pollutants such as detergents and dyes, under UV irradiation [9]. In most of the research paper nanoparticles or nanopowder are used as catalysts for photocatalytic activities. When bulk quantity or powder is used for the photodegradation of organic dyes, complete recovery of the photocatalyst using filtration and centrifugation method is a big challenge [10]. For the solution to this challenge, we have used ZnO thin film instead of powder for photocatalysis. Moreover, thin film photocatalyst has additional advantages than bulk nanomaterials. In order to overcome the problem of rapid recombination of photogenerated electron–hole pairs, ZnO was doped with transition elements, Mn. Moreover, we investigate the effect of change in doping concentration on the photocatalytic activity of ZnO thin film. Vertically grown nanocrystals have more active sites than randomly oriented crystals, for this reason, we tried to synthesize vertically grown nanocrystals on glass substrates.

ZnO nanostructures act as an excellent semiconductor with transition metal dopant because of the exchange

✉ Babasaheb Dole
drbndole.phy@gmail.com

1 Advanced Materials Research Laboratory, Department of Physics, Dr. Babasaheb Ambedkar Marathwada University, Aurangabad 431004, Maharashtra, India

2 Electrical Engineering Department, Nanotechnology and Advanced Material Laboratory, Technology-Educational Institute of Western Greece, Patras, 26500 Patras, Greece

3 UGC-DAE Consortium for Scientific Research, Indore Centre University Campus, Khandwa Road, Indore 452017, India

interactions between the spin of the dopant atoms and the carriers in the ZnO lattice [11]. The doping of transition metal in ZnO was found to increase the efficiency and absorption of a photon [12]. Doping of transition metal ions in ZnO is responsible for the free charge carriers and oxygen vacancies which makes ZnO as a promising material for photocatalytic activity [13]. From recent literature, it was observed that Mn-doped ZnO nanorods have an outstanding photocatalytic performance with high degradation efficiency [14]. The photo-degradation efficiency of ZnO:Mn was significantly higher than that of undoped ZnO. Surface area and crystallinity play an important role in the photocatalytic activities of metal oxides. The reason is that doping of metal oxide with transition metals increases the surface area [15]. Jagpreet Singh et al. reported that Mn–ZnO nanoparticles degraded the dyes more rapidly than the undoped ZnO nanoparticles [16]. Voicu et al. reported that the increase of Mn percentage leads to a better photocatalytic activity, therefore, we have used different doping concentrations of Mn [13].

There are many methods available in the literature for the synthesis of pure and Mn-doped ZnO nanomaterials such as dip coating technique [17], sol–gel and spin coating [18], chemical bath deposition [19], chemical vapor deposition [20], hydrothermal [21], etc. But we have synthesized samples by hydrothermal technique because it is cost effective and viable technique, also it may give different morphology such as nanowires [22], nanorods [23], nano-flowers [24], etc., because of a uniform temperature, pressure and capping agent which were used to synthesize the materials. In this study, Mn-doped ZnO nanorod thin films on glass substrates were synthesized by the one-step hydrothermal method at the same temperatures. For the synthesis of ZnO film in hydrothermal method researchers generally use silicon substrate for growth of ZnO nanorods but in our study, we have used glass substrate instead of silicon because it is cost effective. By this method, we obtained nanorod morphology hence this method is effective to get the fine morphology. We report the growth mechanism of pure and Mn-doped ZnO samples. To study the effect of pure and Mn-doped ZnO samples on the photocatalytic activity the samples were examined qualitatively and quantitatively by different properties such as structural, morphological, chemical bonding, optical and electrical, etc.

2 Experimental

2.1 Sample synthesis

Samples of pure and Mn-doped ZnO nanorod thin films on a glass substrate with chemical formula $Zn_{1-x}Mn_xO$ (x = 0, 0.02, 0.05, 0.08) were prepared by one-step hydrothermal method. For the synthesis of pure ZnO, 1 M Zinc acetate

dihydrate (Fisher Scientific 98.5%) and 1 M Hexamethylenetetramine (HMTA- Fisher Scientific 99%) were dissolved separately in distilled water. The HMTA solution added in Zinc solution under continuous stirring and added ammonia drop-wise to maintain pH to 10 and stirred the solution for 3 h. The glass substrate was firstly ultrasonicated using dilute HCl in an ultrasonic cleaner for 3 h and dried. This substrate was kept vertically aligned in Teflon lined stainless steel autoclave and solution was transferred into the autoclave. Sealed the autoclave and kept in a muffle furnace at 90 °C for 6 h. Cooled the system naturally at room temperature, the deposited film was washed several times with distilled water and dried at room temperature. For the synthesis of Mn-doped ZnO, Zinc acetate dihydrate 1 M, manganese tetrachloride (Fisher Scientific 98–101%) with concentration 2, 5 and 8 mol% and 1 M Hexamethylenetetramine (HMTA) were dissolved separately in 25 ml distilled water respectively. Mixed the above solution with adding ammonia to maintain pH 10 and stirred the solution for 3 h. The cleaned glass substrate was kept into the Teflon lined stainless steel autoclave and solution transferred in the Teflon beaker. Sealed the autoclave and kept in a muffle furnace at 90 °C for 6 h. After cooling the substrate was washed with distilled water and dried at room temperature. Samples were heated at 110 °C for 3 h followed by room temperature (Scheme 1).
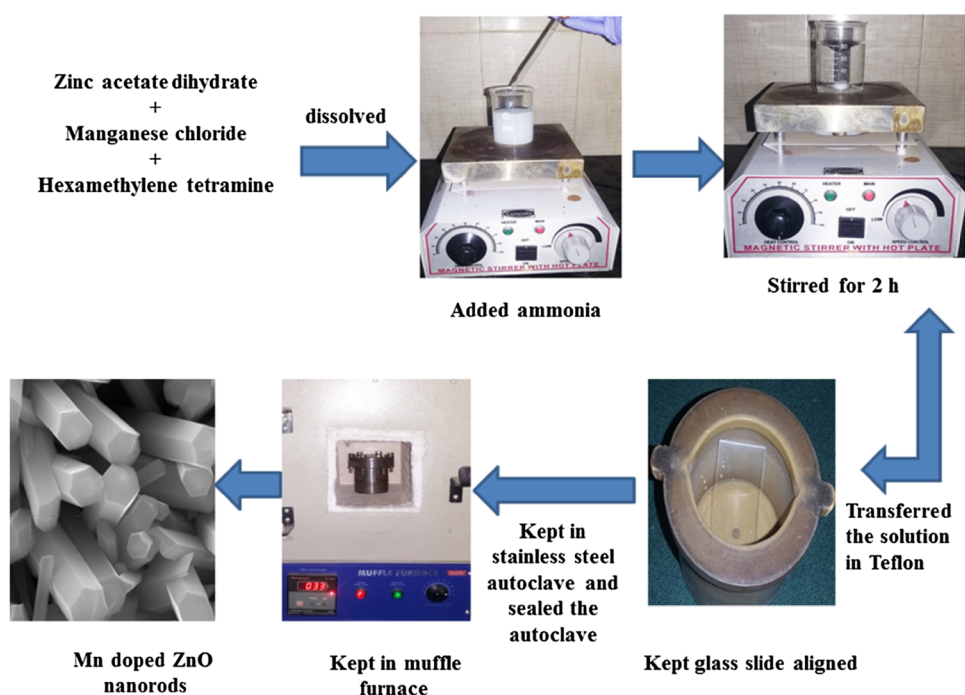
2.2 Photocatalytic degradation procedure

The photocatalytic activity of pure and Mn-doped ZnO nanorods was investigated by the photocatalytic decomposition of Methylene Blue (MB) in an aqueous suspension under UV–Vis light illumination. In a typical experiment pure and Mn-doped ZnO thin film (1 cm × 1 cm) was suspended respectively in an aqueous solution of 0.05 mg MB and 100 ml of deionized water. The catalyst suspension was stirred for 10 min then the sample was kept under a UV lamp (125 W, Nexa Technologies Lelesil). UV–Vis light irradiation was carried out from 0 min to the degradation time of each catalyst. The solution was collected at different time intervals i.e. 20 min and analyzed by absorption spectra in UV–Vis spectroscopy.

2.3 Material characterization

The pure and Mn-doped ZnO thin films were characterized by different techniques. The structural parameter was investigated by XRD using D-8 Advanced diffractometer (Bruker AXS, Germany) with a monochromatic CuK_α radiation source and scintillator detector at a scanning rate of 1° per minute. The Fourier Transform Infra-Red spectroscopy (FT-IR) was measured in the wavelength range of

Scheme 1 Schematic represen-
tation of the synthesis model
of pure and Mn-doped ZnO
nanorods

Zinc acetate dihydrate
+
Manganese chloride
+
Hexamethylene tetramine

dissolved →

Added ammonia

Stirred for 2 h

Transferred
the solution
in Teflon

Kept glass slide aligned

Kept in
stainless steel
autoclave and
sealed the
autoclave

Kept in muffle
furnace

Mn doped ZnO
nanorods

550–4000 cm^{-1} using a Bruker, Germany Model: Vertex 70 spectrometer. The surface morphology and elemental composition were investigated by scanning electron microscope (SEM) and energy-dispersive X-ray analysis (EDAX), respectively, by MIRA II LMH from TESCAN, with a resolution of 1.5 nm at 30 kV. TEM images and selected area electron diffraction patterns were attained for Mn-doped ZnO samples using Tecnai G2 20 at an acceleration voltage of 200 kV. The absorption spectrum was examined using a UV–Vis spectrometer (Avantes spec with fiber optic). Fluorescence spectra of pure and Mn-doped ZnO were scrutinized using UV–Vis spectrometer (Avantes spec with fiber optic). I–V characteristic of prepared sample was carried out by using the semiconductor parameter analyzer, model: Keithley-4200 A. The Raman spectra of pure and Mn-doped ZnO nanorods were registered by using an Ar ion laser with 514.5 nm wavelength and 50 mW powers as the excitation source. The specific surface area, pore radius and pore volume of the pure and Mn-doped ZnO nanorods were explored with Quanta chrome ASiQwin 1994-2017 BET Autosorb iQ instrument system using the dynamic Brunner–Emmet–Teller (BET) method in which N_2 gas was adsorbed at 77.35 K. The qualitative identification of the pure and Mn-doped ZnO and photocatalytic degradation reaction of pure and Mn-doped ZnO samples were inspected by high-performance methylene blue liquid using a Lelesil Innovative Systems photochemical refractometer instrument with UV lamp (125 W).
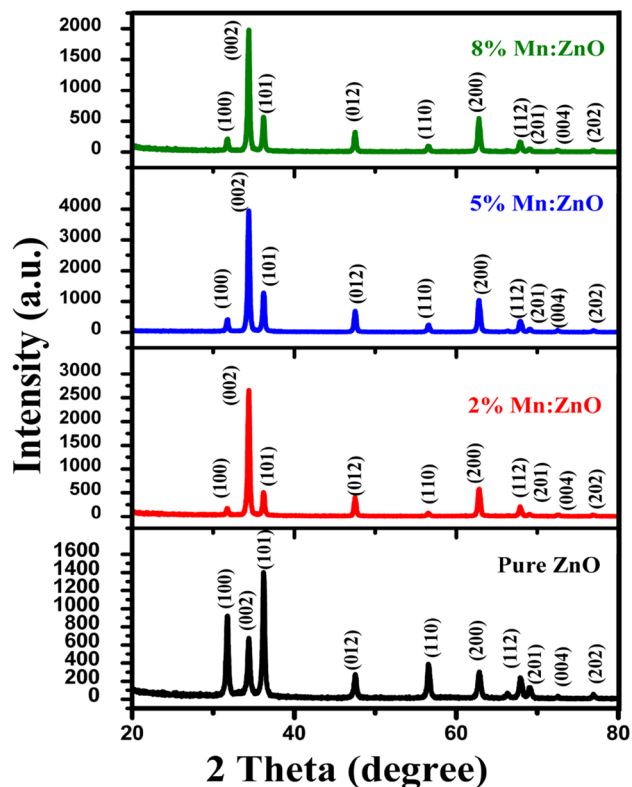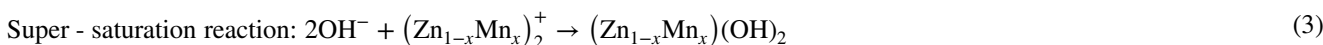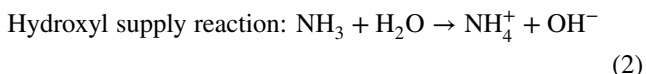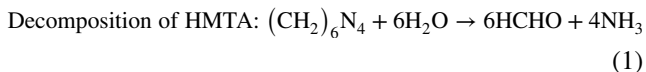
Fig. 1 XRD patterns of pure and Mn-doped ZnO nanorods

2.4 Growth mechanism

The XRD results (Fig. 1) of pure and Mn-doped ZnO samples revealed vertical growth of nanorods along the (002) plane due to the suppression along with the [0001] direction because as prepared Mn-doped ZnO nanorods have nonpolar in nature with the $[10\bar{1}0]$ as shown in Fig. 1. The strong and dominant (002) peak indicated the preferred orientation of the pure and Mn-doped ZnO along with the [0001] direction [25]. During the solution growth of pure and Mn-doped ZnO nanorods, hexamethylenetetramine (HMTA) of purity 99% ($(CH_2)6N_4$) were used as the capping agent. Growth orientation along (002) plane was due to the HMTA which controls the growth along [0001] and capping along with the $[10\bar{1}0]$ direction [26]. Thus growth along the (100) plane goes on decreasing while increasing along (002) plane. This effect became more significant as the Mn content increased, leading to increasing the length of nanorods because Mn reacts as a metal catalyst which helps to the growth of Mn-doped ZnO nanorods. Zinc acetate dihydrate with purity 99% ($Zn(CH_3COO)_2 \cdot 2H_2O$) and manganese chloride was used as precursor and ammonia NH_4 was used to maintaining the pH at 10. The chemical reactions of pure and Mn-doped ZnO nanorods are as follows [27]:

Decomposition of HMTA: $(CH_2)_6N_4 + 6H_2O \rightarrow 6HCHO + 4NH_3$ (1)

Hydroxyl supply reaction: $NH_3 + H_2O \rightarrow NH_4^+ + OH^-$ (2)

Super - saturation reaction: $2OH^- + (Zn_{1-x}Mn_x)_2^+ \rightarrow (Zn_{1-x}Mn_x)(OH)_2$ (3)

Nanorods growth reaction of Mn-doped ZnO samples in the hydrothermal autoclave:

$(Zn_{1-x}Mn_x)(OH)_2 \rightarrow Zn_{1-x}Mn_xO + H_2O$ (4)
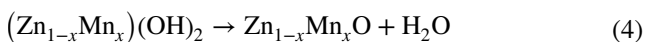
3 Results and discussion

3.1 Crystallographic analysis

The structural investigation of pure and Mn-doped ZnO were scrutinized using XRD technique as shown in Fig. 1. The X-ray diffraction peaks at (100), (002), (101), (012), (110), (013), (200), (112), (201) and (004) exhibit the formation of hexagonal wurtzite structure [28]. These diffraction peaks were well matched with the Joint Committee on Powder Diffraction Standard (JCPDS) card

no. 96-900-4180 with a = 0.3250 nm and c = 0.5205 nm. Peaks of (100), (002) and (101) at 2θ = 31.74, 34.42 and 36.24, respectively, which indicate that the samples are crystalline in nature. No extra peaks of secondary phases were detected for pure and Mn-doped ZnO samples. From XRD results, the intensity of pure and Mn-doped ZnO was increased with increasing the doping concentration of Mn in ZnO up to 5%, but it was decreased for 8% due to the solubility limit of Mn-doped ZnO lattice. The metal dopant (Mn) acts as a catalyst for the growth of ZnO nanorods. The (002) plane with (0001) direction in ZnO lattice is minimum energy plane thus preferred orientation in our system is along (002).

The average crystallite size was calculated by Debye–Scherrer's formula [29]:

$$D = \frac{K\lambda}{\beta \cos \theta}$$ (5)

The change in crystallite size with Mn concentration confirms the incorporation of an Mn^{2+} ion at the Zn^{2+} site of ZnO structure [30]. Figure 2a–d show that full Rietveld refinement of pure, 2, 5, and 8% Mn-doped ZnO nanorods respectively which demonstrated that all samples are consistent with the wurtzite structure. The refinement results for all samples were summarized in Table 1. The lattice parameters a and c were calculated by using the following formula [31].

$$\frac{1}{d^2} = \frac{4}{3}\left[\frac{h^2 + hk + k^2}{a^2}\right] + \frac{l^2}{c^2}$$ (6)

where a and c are the lattice constants and d is the interplanar spacing between planes and Miller indices (h, k, l). The calculated values of lattice parameters show slight changes due to Mn doping. Atomic packing fraction (APF) of bulk ZnO is 74% but in our case, for pure and Mn-doped ZnO samples it was found to be 75% it may be due to nanorod size effect in samples [30]. From Table 1 it was confirmed that volume changes with Mn concentration, it is due to variation in lattice parameters with Mn concentration. u parameter was calculated using the following formula,

$$u = \frac{a^2}{3c^2} + 0.25$$ (7)

u parameter was changed with increasing Mn concentration it may be due to the variation in lattice parameter.

The bond length (L) was scrutinized using the following formula [32],

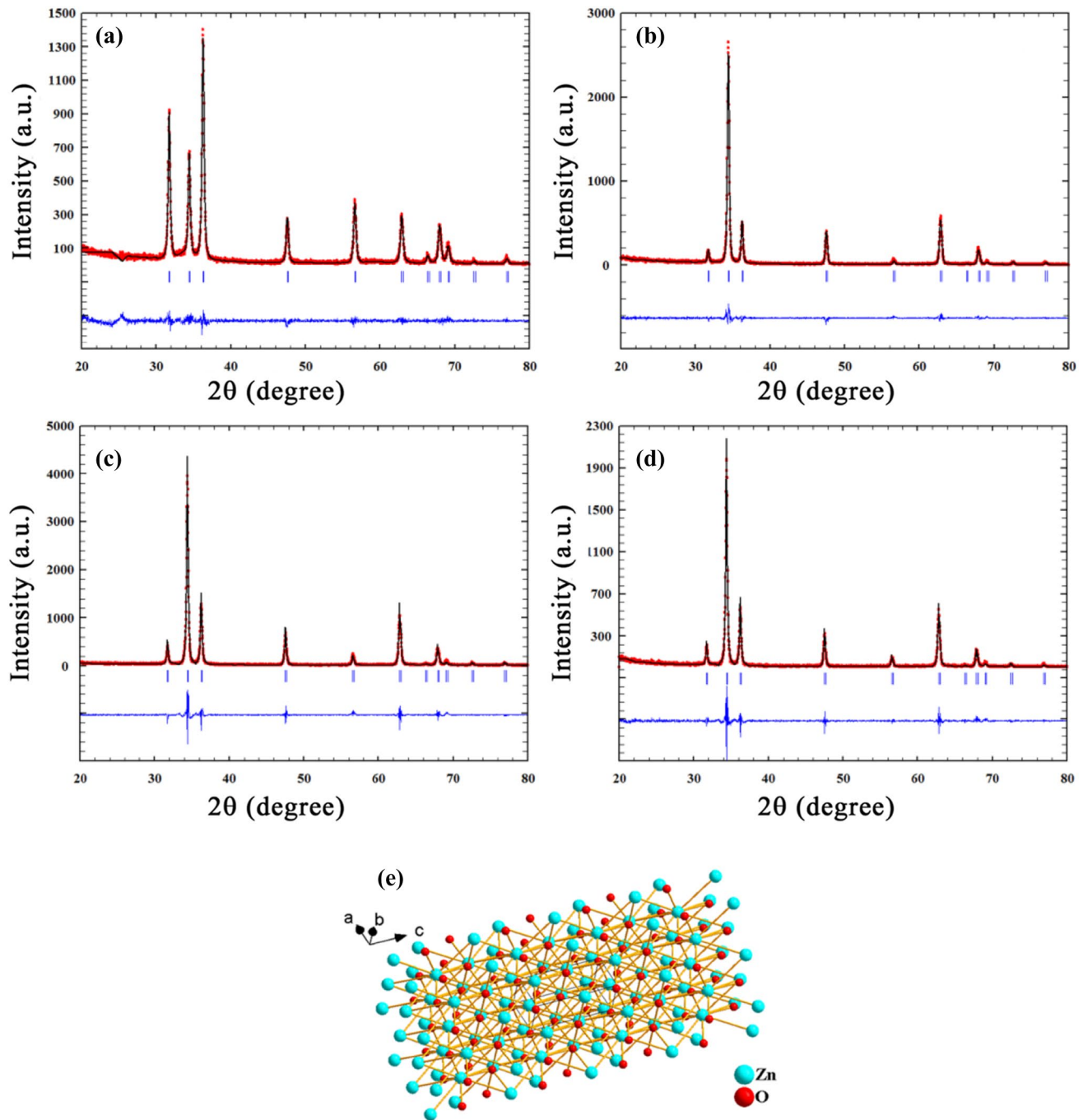$$L = \sqrt{\frac{a^2}{3} + \left(\frac{1}{2} - u\right)^2 c^2}$$ (8)

Fig. 2 Rietveld refinement of pure and Mn doped ZnO nanorods with concentrations **a** 0%, **b** 2%, **c** 5%, **d** 8% and **e** representative crystal structure of ZnO nanorods

From Table 1 it was explicitly corroborated that bond length increased with increasing Mn concentration in ZnO lattice. A slight change was traced in c/a ratio of pure and Mn-doped ZnO was due to the variation in values of lattice parameters. The crystallinity of pure and Mn-doped ZnO samples was clearly observed from the ratio of (100) and (002) planes peak intensity. From XRD results it was explicitly found that the 5% Mn-doped ZnO sample has higher crystallinity than other samples which are useful to the photocatalytic activity. Figure 2e represents the ZnO crystal structure simulated from Rietveld refinement of pure ZnO sample.

Table 1 Lattice parameter, crystallite size, APF, volume of unit cell, u parameter, bond length and c/a ratio

Sample	Lattice parameter (nm)		Crystallite size	APF	Volume of unit cell ($\mathring{A}$)^3	u parameter	Bond length ($\mathring{A}$)	c/a ratio
	a($\mathring{A}$)	c($\mathring{A}$)						
ZnO	3.2500	5.2062	27.1946	0.7548	47.6240	0.379898	1.9778	1.6019
2% MZO	3.2518	5.2009	30.1025	0.7560	47.7094	0.380307	1.9779	1.5993
5%MZO	3.2513	5.2091	31.7953	0.7547	47.6870	0.379858	1.9787	1.6021
8%MZO	3.2529	5.2116	29.1384	0.7547	47.7599	0.379861	1.9796	1.6021
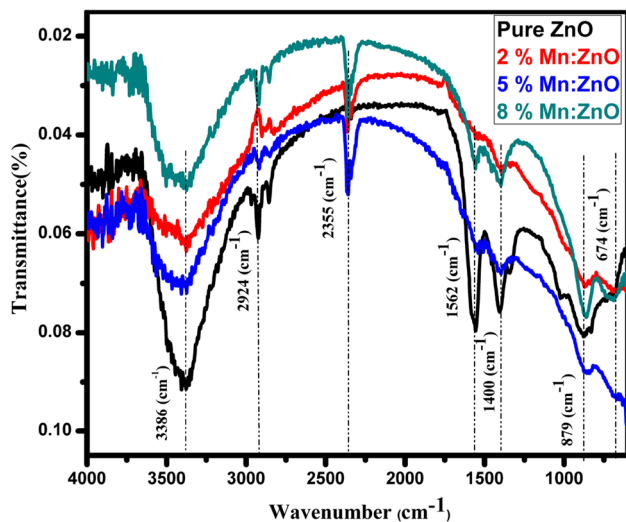
Fig. 3 FT-IR Spectra of Pure and Mn-doped ZnO nanorods

3.2 FTIR spectroscopy

FTIR spectra were used for detection of functional groups and chemical bonds in the pure and Mn-doped ZnO nanorods. Figure 3 shows a broad peak of O–H stretching in the higher energy region at 3386 cm^{-1}. FTIR spectra of a pure sample of the present investigation are similar to that of Mn-doped ZnO samples and are in good agreement with the reported values [30]. The peak around 2924 cm^{-1} shows that asymmetric and symmetric vibration of C–H respectively. The bands appeared near at 2355 cm^{-1} indicates the atmospheric CO_2 adsorption on the surface of the oxide. The band at 1562 cm^{-1} indicates the asymmetrical and symmetrical stretching modes of the carboxylate groups of residual acetate anions chemically attached to the sample surface during the synthesis process [33]. The band at 1400 cm^{-1} attributed to the C–H bending and angular deformation of C–H bond in the starch molecule, respectively [34]. Similarly, the band at 879 cm^{-1} indicates the formation of Zn–O bonds [33]. The peak at 674 cm^{-1} corresponds to Mn–O stretching [35]. The peaks were observed in FT-IR spectra due to the capping of HMTA but these peaks of capped HMTA do not affect on photocatalytic degradation of MB [36].

4 Morphological study

4.1 Scanning electron microscopic (SEM)

Scanning electron microscopy (SEM) is one of the promising techniques for the surface morphological study of the samples and it gives important information about the shape and size of the nanorods. SEM images of pure and Mn-doped ZnO nanorods with different concentration of Mn are shown in Fig. 4. It was observed before doping of Mn, the sample have regular, uniformly grain-sized and hexagonal shaped nanoparticles. For 2, 5 and 8% Mn-doped ZnO samples cylindrical shaped nanorods with hexagons at top of the rod were observed. SEM images show that the prepared nanorods are mostly vertically aligned corresponding to the substrate. Mn-doped ZnO samples show maximum changes in the morphology, which is due to the Mn act as a metal catalyst which helps to growth of single crystal [37]. The metal catalyst in crystal growth may be staying at the surface of material or bottom of the material and helps to growth of single crystalline material. Formation of rods for Mn-doped ZnO samples which were due to combination or aggregation of particles. SEM image of 5% Mn-doped ZnO nanorods shows the needle-like structure at the surface which indicates surface defects are present on sample surface which may play an important role in photocatalytic activity.

4.2 EDAX analysis

EDAX spectra of pure and Mn-doped ZnO nanorods are displayed in Fig. 5a–d, illustrating the presence of elements in the samples. Elemental compositions of pure and Mn-doped ZnO samples are summarized in Table 2. The EDAX spectra of pure ZnO nanorods show Zn and O elements. The atomic concentration of Zn and O ions in pure ZnO sample was 44.97% and 55.03% respectively. In 2% Mn-doped ZnO sample atomic percentage of Zn is 42.06%, oxygen 57.70% while Mn is not observed on the surface of the rod it may be due to Mn substitutes at the lateral site or interstitial site of host ZnO. But 0.24% Calcium was observed in 2% Mn-doped ZnO sample due to the contamination during the measurement of SEM and EDAX. In 5% Mn-doped ZnO sample atomic concentration of Mn, Zn and O are 3.41,

Fig. 4 SEM images of pure and Mn doped ZnO nanorods with Mn concentration: **a** 0%, **b** 2%, **c** 5%, **d** 8%
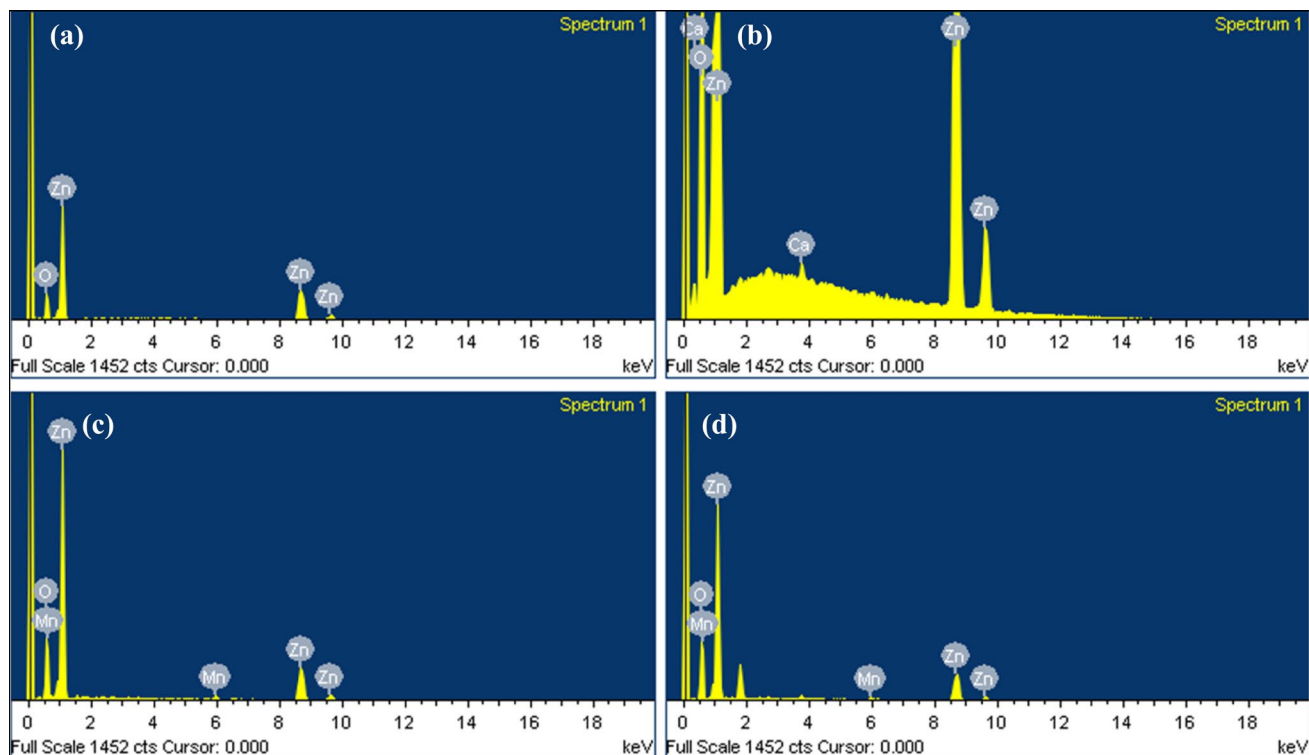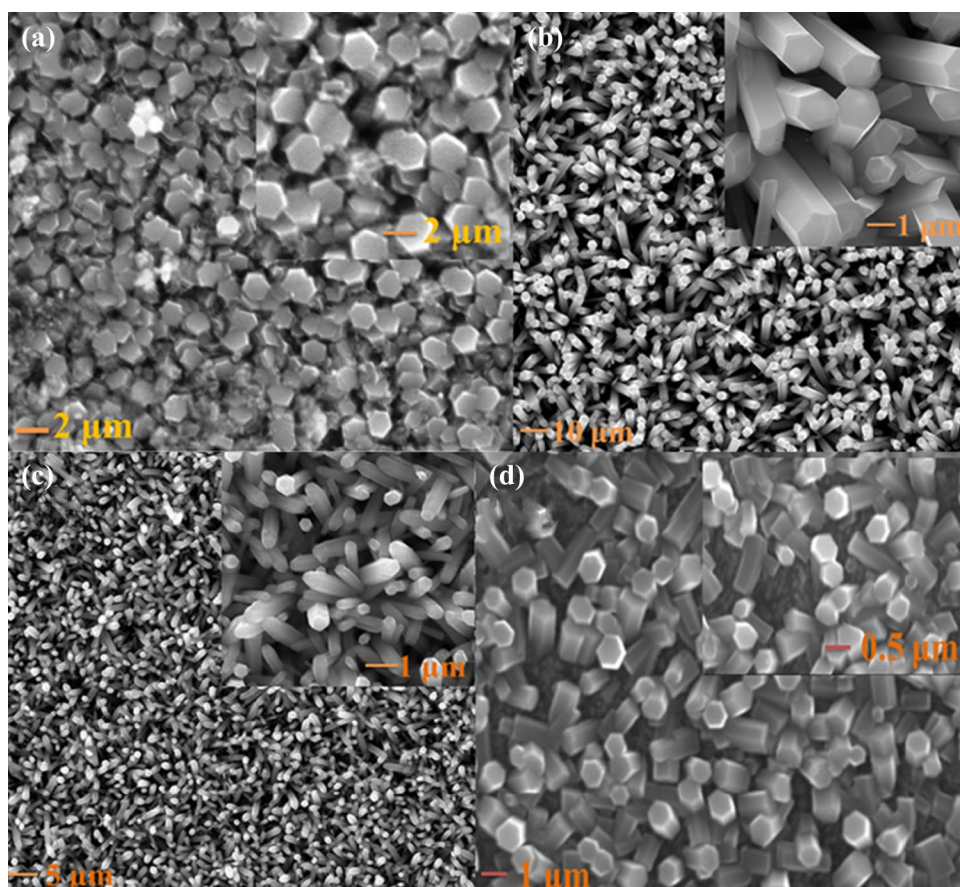

Fig. 5 EDAX micrographs of **a** pure, **b** 2%, **c** 5% and **d** 8% Mn doped ZnO nanorods

Sample	Zn (%)	O (%)	Mn (%)	Elemental total %
Pure ZnO	44.97	55.03	–	100
2% Mn:ZnO	42.06	57.70	–	100
5% Mn:ZnO	30.23	66.36	3.41	100
8% Mn:ZnO	27.93	65.90	6.17	100

30.23, and 66.36% respectively. Similarly, for 8% Mn-doped ZnO sample elemental composition was found 6.17% Mn, 27.93% Zn and 65.90% O. It was found that Mn has been substituted in ZnO matrix.

4.3 Transmission electron microscopy

Figure 6 shows the morphology and microstructure of pure and Mn-doped ZnO samples. From Fig. 6a it was observed that pure ZnO sample exhibits morphology as nanoparticles while (b) 2%, (c) 5% and (d) 8% Mn-doped ZnO samples show the formation of nanorods. The particle size of pure ZnO nanoparticles was 37.73 nm while from XRD calculation it was 27.19 nm. Length of 2, 5, and 8% Mn-doped ZnO nanorods was found 3338 nm, 4443 nm and 2246 respectively. The average diameter was calculated from TEM data which shows for 2, 5 and 8% Mn-doped ZnO nanorods in the range 300–350 nm respectively [38]. From the calculations of length and diameter, it was observed that the diameter of nanorods was the same while the length was changed as varying the Mn content in ZnO. It was clearly confirmed that from TEM images the increases in length of nanorods with increasing Mn content, it is might due to the Mn metal catalyst which helps to the growth of nanorods [39]. TEM images show 5% Mn doped ZnO nanorods have higher in length than all samples which was also observed in XRD patterns. The selected area electron diffraction pattern of the Mn-doped ZnO shows a single crystal structure of the nanorods. The SEAD images show a dot and circular ring-like patterns, which indicate the high crystallinity of the nanorods. The indexing of the SAED patterns shows the existence of lattice planes such as (002), (101), (103), (012), (110) and (200) which were clearly shown in the XRD patterns. Zhang et al. reported that average length of ZnO nanorods was 800 nm while in our case Mn-doped ZnO nanorods are longer than reported values i.e. 4443 nm which may play an important role in photocatalytic activity [9].

4.4 Diffuse reflectance spectroscopy (DRS)

UV–Vis spectroscopy has been used to investigate the optical properties of the pure and Mn-doped ZnO nanorods. Reflectance spectroscopy is a powerful non-destructive technique to have a better understanding of the effect of Mn doping on the optical properties of ZnO nanorods. The diffuse reflectance spectra of pure and Mn-doped ZnO samples are shown in Fig. 7a. Strong reflections were found above

Fig. 6 Transmission electron microscopy images and SAED pattern image of pure and Mn-doped ZnO nanorods with Mn concentration: **a** 0%, **b** 2%, **c** 5%, **d** 8%
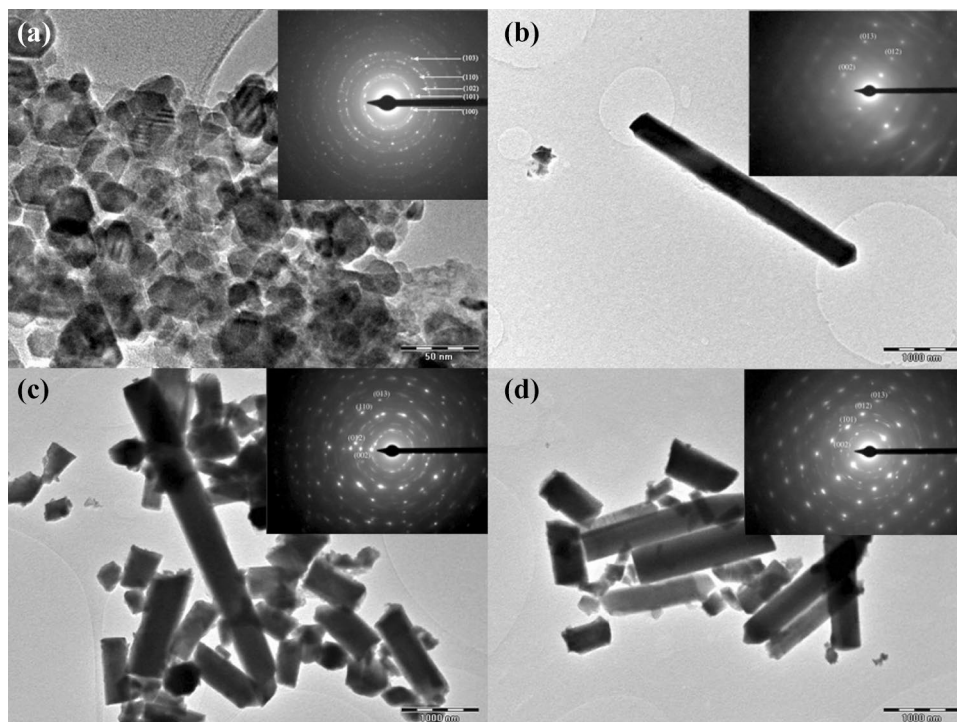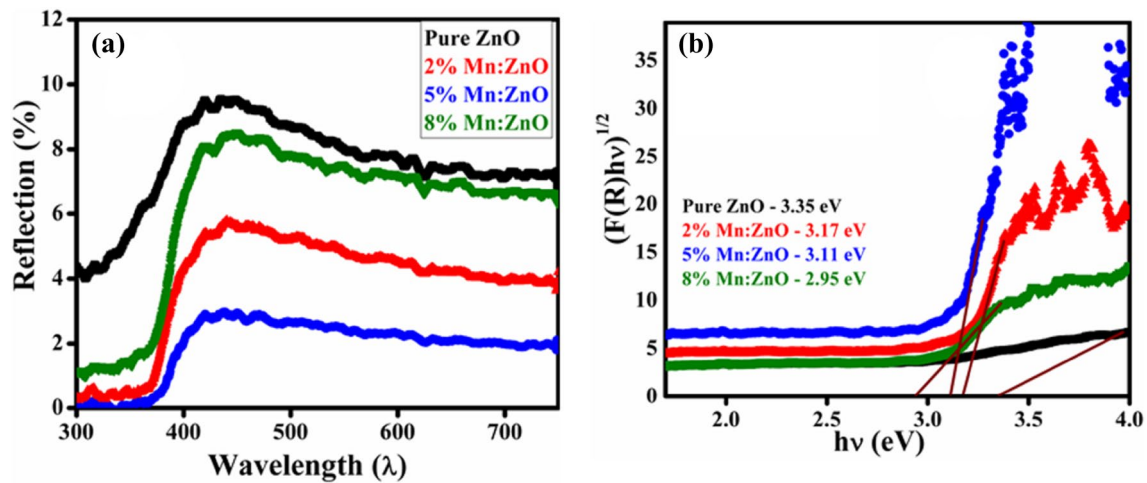
Fig. 7 **a** UV–Vis reflectance spectra and **b** Energy band gap of Pure, 2%, 5%, 8% Mn-doped ZnO nanorods

400 nm for all samples. The absorbance was calculated using the Kubelka–Munk equation [40]:

$$\frac{K}{S} = \frac{(100 - R)^2}{2R} = F(R) \tag{9}$$

F(R) is the remission or Kubelka–Munk function. If the material scatters in a perfectly diffuse manner, the K–M absorption coefficient K becomes equal to 2α. The band gap E_g and coefficient (α) of a direct band gap for semiconductor are related by following equation [41].

$$\alpha h\upsilon = B\left(h\upsilon - E_g\right)^{\frac{1}{2}} \tag{10}$$

where α is the linear absorption coefficient, B is the constant, E_g is the energy gap, υ is the frequency of the incident radiation and h is Planck's constant. In this case, considering the K–M scattering coefficient S as a constant with respect to the wavelength, and using the remission function in Eq. (9), we obtain the expression:

$$[F(R)h\upsilon]^2 = B\left(h\upsilon - E_g\right) \tag{11}$$

The energy bandgap of all samples was measured by plotting the graph of $[F(R)h\upsilon]^2$ versus hυ as shown in Fig. 7b. The energy band gap of pure, 2, 5 and 8% Mn doped ZnO was found to be 3.35 eV, 3.17 eV, 3.11 eV, 2.95 eV respectively. Doping of Mn revealed a decrement in the band gap with increasing Mn concentration, acknowledges the red shift. Decrement in energy band gap is due to the enhancement in the crystallite size of samples. From this, one may conclude that the decrease in energy band gap facilitates the electron can easily pass from valence band to conduction band and therefore increase in the electron flow in the Mn doped ZnO sample as compared to pure ZnO [42]. The

decrement in the energy band gap is one of the important parameters to improve the photocatalytic performance [43].

4.5 Fluorescence study

The fluorescence spectrum of Mn-doped ZnO nanorods was taken in the range 300–750 nm, which is called a band edge emission region. This emission could be related to the recombination of electrons from the valence band and holes from the conduction band [44]. This spectrum was taken for the comparative study of fluorescence intensity between the pure and Mn-doped ZnO nanorods. Figure 8 shows the fluorescence emission spectra of pure and Mn-doped ZnO nanorods which were observed in the range 375–700 nm. The strong ultraviolet emission spectra of narrow violet (388 nm) were observed for the pure and Mn-doped ZnO nanorods. Broad green emission band in the visible region at 527–563 nm which was due to different intrinsic or extrinsic
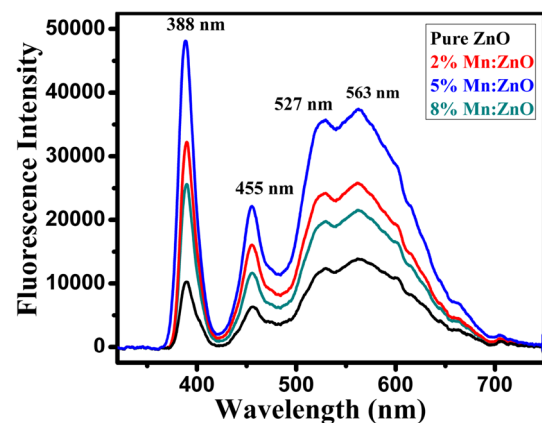

Fig. 8 Fluorescence spectra of pure, 0, 2, 5, and 8% Mn-doped ZnO nanorods

defects and surface or oxygen vacancy defects [9]. Fluorescence is closely related with the recombination of the electron–hole pairs. Surface defects and oxygen vacancy may enhance the electron–hole pair separation rate in Mn-doped ZnO nanorods. The visible emission spectrum of pure ZnO nanorods shows the low intensity but after the doping of Mn in ZnO reveals remarkable changes in the intensity of visible emission peaks. The intensity was increased for Mn doping in ZnO nanorods. From blue and green emission spectrum fluorescence intensity of 5% Mn-doped ZnO nanorod has higher than all samples. Enhancement in green emission intensity suggesting the abundant surface oxygen vacancies or presence of more defects in 5% Mn-doped ZnO nanorods which may play a vital role in the photocatalytic activity [9].

4.6 I–V characteristics

Room temperature current versus voltage (I–V) characteristics of pure and Mn-doped ZnO samples is shown in Fig. 9. I–V measurement of pure and Mn-doped ZnO nanorods was carried out by using a drop casting method. Nanorods were detached from the surface of the substrate for I–V measurement. In Fig. 9 all curves are passing through origin exhibiting ohmic nature of the pure and Mn-doped ZnO nanorods. The electrical resistance for pure ZnO sample was 266 MΩ which was determined from the inverse slope of the curve. The electrical resistance for 2, 5, and 8% Mn-doped ZnO samples was found to be 1.39 MΩ, 1.22 MΩ, and 1.53 MΩ respectively. The electrical resistance was decreased with increasing Mn concentration up to 5% Mn doping in ZnO owing to the enhancement in crystallinity. For 8% Mn-doped ZnO nanorods the electrical resistance was slightly increased which may be due to the reduction in crystallinity. Resistance was explicitly suppressed for 5% Mn-doped ZnO sample whereas conductivity enhanced drastically it may be owing to the reduction in voids and
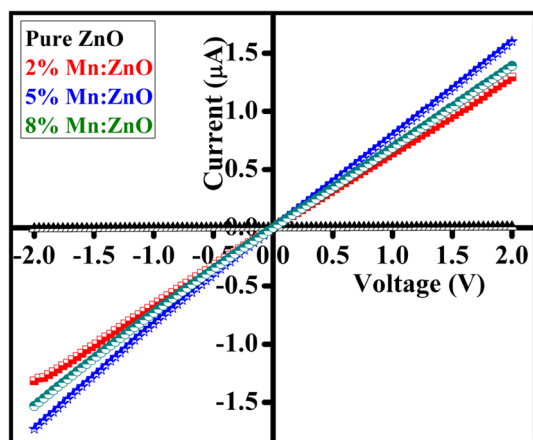

Fig. 9 Current–voltage curves of pure and Mn-doped ZnO nanorods

vertically oriented crystallites in ZnO lattice. It was attributed that the enhancement in crystallinity for Mn-doped ZnO samples leads to improvement mobility and reduces the scattering of carriers at grain boundaries [45]. Thus increased in conductivity is due to doping of Mn in ZnO lattice.

4.7 Raman spectroscopy

Raman spectroscopy is commonly used to investigate the chemical compositions, defect states, and lattice dynamics of materials. ZnO is a polar crystal belonging to wurtzite structure with point group C_{6v} in which both Zn and O atoms occupying C_{3V} sites. The Brillouin zone at (Γ point) predicts that the lattice optical phonon modes have the following representation [46]:

$$\Gamma_{opt} = A_1 + 2B_1 + E_1 + 2E_1 \tag{12}$$

where A_1 and E_1 are polar modes and both are infrared and Raman active, while E_2 modes are non-polar. The non-polar E_2 modes have two wave numbers, namely, E_2^{high} and E_2^{low} associated with the motions of oxygen and Zn sub-lattice, respectively. Raman spectra of pure and Mn-doped ZnO were observed in the range 200–800 cm^{-1} as shown in Fig. 10a. The longitudinal optical (LO) and transverse optical (TO) phonon scattering peaks were shown in Fig. 10a. We have observed for pure ZnO and Mn-doped nanorods common phonon modes centered at 336.16, 383.21, 439.70 and 582.30 cm^{-1} corresponding to $E_2^{high} - E_2^{low}$, A_1^{TO}, E_2^{high}, and A_1^{LO} respectively. The E_2^{high} and A_1^{LO} modes of wurtzite structure for pure and Mn-doped ZnO are allowed and observed thus; one may conclude that Raman spectra indicate wurtzite structure which was confirmed by XRD. As Mn doping increases, the E_2^{high} mode slightly shifted towards the higher frequency from 439.70 to 440.52 cm^{-1} due to the doping effect which was shown in Fig. 10b [47, 48]. In Raman spectra shifting of peaks towards lower or, higher wavenumber is due to the chemical bonds and symmetry of atoms. Hence changes in chemical bond length cause wavenumber shifting owing to Mn doping into ZnO lattice.

4.8 BET surface analyzer

It is widely believed that the degradation efficiency of photocatalytic activity is more dependent on the specific surface area of the photocatalyst. The nitrogen adsorption–desorption isotherms and the pore size distribution plots of pure and Mn-doped ZnO nanorods are as shown in Fig. 11. The surface area of pure and Mn-doped ZnO thin films (1 cm × 1 cm) was measured using the BET technique. The isotherms were identified as type-V adsorption isotherm with an extended S-type hysteresis loop indicating unrestricted multilayer formation process implying the existence of cylindrical-shaped and slit-shaped pores, which suggests that the samples are
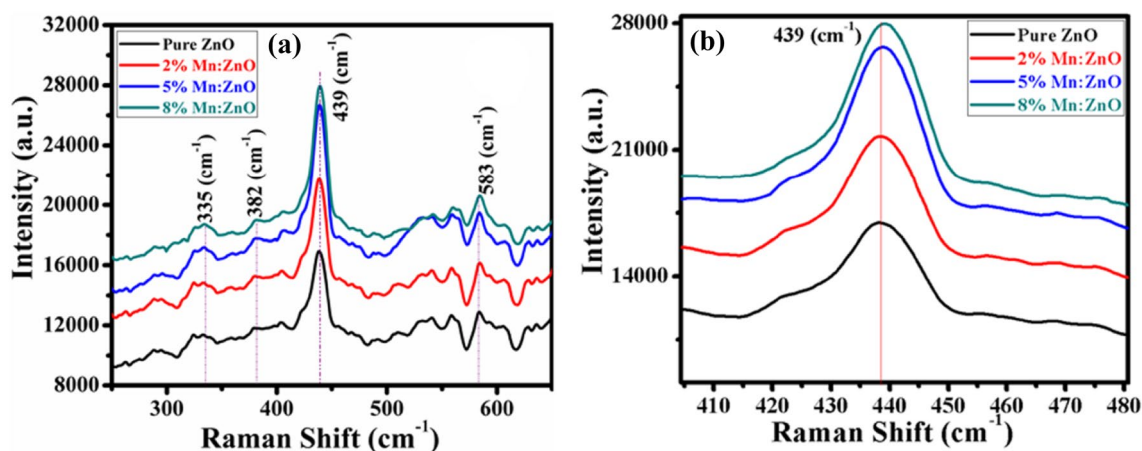
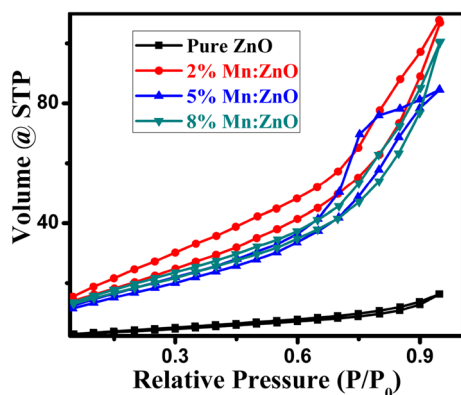**Fig. 10** **a** Raman spectra of pure and 2%, 5%, 8% Mn-doped ZnO nanorods. **b** Zoom Plot of E_2^{high}

Fig. 11 N_2 adsorption–desorption isotherms of the pure and Mn-doped ZnO nanorods with concentration 0, 2, 5, and 8% photocatalysts

Table 3 Values of surface area, pore volume and pore diameter of pure and Mn-doped ZnO nanorods

Sample	Surface area (m²/g)	Pore volume (cc g⁻¹)	Pore diameter (nm)
Pure ZnO	14.694	0.026	6.88
2% Mn:ZnO	78.983	0.1308	8.23
5% Mn:ZnO	63.598	0.1653	8.37
8% Mn:ZnO	68.549	0.1555	9.08

mesoporous according to the IUPAC classification [49]. The pure and Mn-doped ZnO samples exhibit a typical characteristic mesoporous structure, which was confirmed by the N_2 gas adsorption. The BET surface area, pore volume, and pore diameter were calculated by the BJH method for pure and Mn-doped ZnO nanorods and these values are depicted in Table 3. From the present investigation, it was evidently corroborated that average surface area was enhanced as doping

of Mn content in ZnO lattice whereas for 2% it is higher. Furthermore, it was verified that more pores are present in 2% Mn-doped ZnO sample. Ahmad et al. reported that the specific surface area for 1, 3, and 5% was 44.9 m²/g, 46.2 m²/g and 47.8 m²/g respectively whereas our results for 2, 5, and 8% Mn-doped ZnO nanorods have obtained higher values of specific surface area, it may be owing to nucleation of Mn ions into ZnO lattice and Mn clustering [50]. 2% Mn-doped ZnO sample shows higher surface area compare to other samples because the surface of minimum energy plane (002) is higher. This minimum energy surface adsorbs more N_2 gas compare to another sample; therefore, the surface area of 2% Mn-doped ZnO sample is larger than other samples. Increases in surface area can be attributed to the creation of new pores due to Mn doping in ZnO lattice.

4.9 Photocatalytic degradation studies

Methylene blue is a one of the difficult naturally degradable dye, to degrade the methylene blue we have performed the photocatalytic activities of the prepared sample. The photocatalytic activity was evaluated by the degradation of methylene blue (MB) in an aqueous system under UV–Vis light irradiation using 1 cm×1 cm thin films of pure and Mn-doped ZnO. Figure 12 shows the time evolution of the UV–Vis spectra of MB solution at about 650.04 nm in the photodegradation experiment with and without a catalyst. Figure 13a shows the plot of the photodegradation percentage with varying irradiation time. The photodegradation efficiency in (%) is defined as the maximum photodegradation at 100 min was calculated by the following relation:

$$\text{Photodegradation efficiency (\%)} \left(\frac{C_0 - C_{100}}{C_0} \right) \times 100 \quad (13)$$

Fig. 12 Time-dependent absorption spectra of MB solutions in the presence of **a** Pure ZnO and **b** 2%, **c** 5% and **d** 8% Mn doped ZnO nanorods
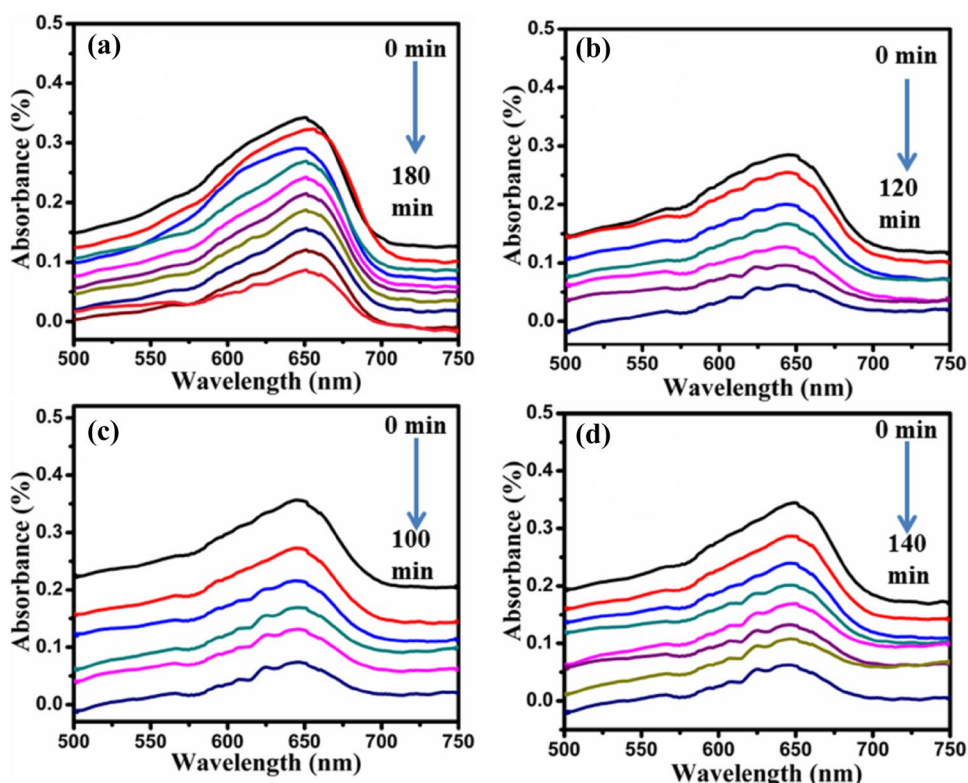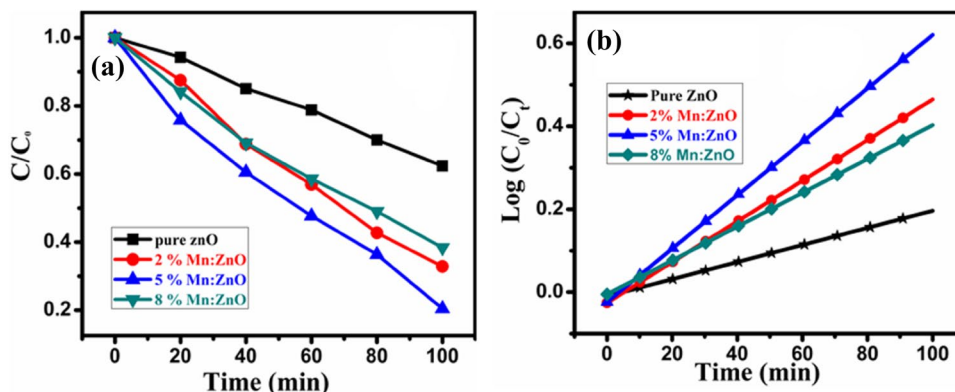

Fig. 13 **a** Plots of C/C$_0$ versus time (t) using different photocatalysts. **b** Plots of $\log \frac{C_0}{C_t}$ versus irradiation time for the different concentration of Mn doped ZnO nanorods

Here, the change between the values of C$_0$ and C$_{100}$ which was the initial (at t = 0) and final (at t = 100 min). Peak heights for the characteristic MB UV–Vis absorption were estimated using the catalyst of pure and Mn-doped ZnO nanorods thin film respectively. Photodegradation efficiency and Pseudo-first-order rate constant of pure and Mn doping ZnO nanorod thin films are depicted in Table 4. It was explicitly corroborated that for 5% Mn-doped ZnO sample has the higher photodegradation efficiency than other samples it may be due to the effective transportation of charge carriers to the length of the nanorods [51]. Kinetic studies were performed for pure and Mn-doped ZnO samples which results are shown in Fig. 13a, b. Our samples follow

Table 4 Results of photodegradation efficiency (%) and Pseudo-first-order rate constant (k) of pure and Mn-doped ZnO nanorods

Sample	Photodegradation efficiency (%)	Pseudo-first-order rate constant (k)
Pure ZnO	38	0.0931
2% Mn:ZnO	66	0.2196
5% Mn:ZnO	79	0.2981
8% Mn:ZnO	61	0.1988

pseudo-first-order kinetics relation for photodegradation of methylene blue the relation is given below [51],

$$\log \frac{C_0}{C_t} = kt \tag{14}$$

where C_0 at Time = 0 and C_t at time = 100, respectively, k is the pseudo-first-order rate constant. The rate constant (k) was calculated using the slope of the plot of $\log \frac{C_0}{C_t}$ versus irradiation time. It was observed that 5% Mn doped ZnO sample has higher rate constant than all samples. Nanowires with large surface area usually have more active sites to absorb organic molecules for photodegradation. 2% Mn doped ZnO nanorods has larger surface area than other samples but surface defects, length and crystallinity of 5% Mn doped ZnO nanorods was higher than all samples therefore it has higher degradation efficiency and higher rate constant. Ma et al. reported that methylene blue was degraded 90% in 4 h. In our case degradation efficiency was found to be 79% for 100 min which fortifies that rate constant was faster than reported results [52]. A high degree of crystallinity is often required rather than a high surface area for photodegradation of dyes because it cases lower recombination between photogenerated electrons and holes.

5 Conclusions

Mn-doped ZnO nanorods were successfully synthesized by a one-step hydrothermal method. Pure and Mn-doped ZnO nanorods exhibit wurtzite structure. In the X-ray diffraction patterns (002) plane shows the growth orientation of as-prepared nanorods. Presence of functional groups in FT-IR spectra show formation of ZnO and Mn doped ZnO. Length and diameter of pure and Mn-doped ZnO nanorods were found in the range 1–4 μm and 300–350 nm respectively. UV–Vis spectra shows the energy band gap was decreased as Mn content increased which acknowledges the red shift. The fluorescence spectrum of Mn-doped ZnO nanorods shows green emission band which indicates defects are present in the samples. From I–V results the conductivity of 5% Mn-doped ZnO sample was better than all samples owing to higher crystallinity. A strong ZnO band was observed from the Raman spectra for pure and Mn-doped ZnO nanorods which were shifted from 439 to 440 cm^{-1}. BET investigations were corroborated that 2% Mn-doped ZnO sample has a higher specific surface area. From photocatalytic activity result, 5% Mn-doped ZnO sample shows higher photodegradation efficiency (%) and higher Pseudo-first-order Rate constant due to the enhancement of length and defects in nanorods.

References

1. P. Kaur, S. Kumar, C.L. Chen et al., Appl. Phys. A Mater. Sci. Process. (2016). https://doi.org/10.1007/s00339-016-9707-5
2. M. Rouchdi, E. Salmani, B. Fares, N. Hassanain, A. Mzerd, Results Phys. **7**, 620 (2017). https://doi.org/10.1016/j.rinp.2017.01.023
3. J.S. Malhotra, A.K. Singh, R. Khosla, S.K. Sharma, G. Sharma, S. Kumar, J. Mater. Sci. Mater. Electron. **29**, 3850 (2018). https://doi.org/10.1007/s10854-017-8321-4
4. M.-T. Chen, M.-P. Lu, Y.-J. Wu et al., Nano Lett. **10**, 4387 (2010). https://doi.org/10.1021/nl101907h
5. C. Klingshirn, R. Hauschild, J. Fallert, H. Kalt, Phys. Rev. B **75**, 115203 (2007). https://doi.org/10.1103/PhysRevB.75.115203
6. R. Majithia, S. Ritter, K.E. Meissner, Anal. Chim. Acta **812**, 206 (2014). https://doi.org/10.1016/j.aca.2014.01.012
7. A. Echresh, C. Chey, M. Shoushtari, V. Khranovskyy, O. Nur, M. Willander, J. Alloys Compd. **632**, 165 (2015). https://doi.org/10.1016/j.jallcom.2015.01.155
8. C.E. Small, S. Chen, J. Subbiah et al., Nat. Photonics **6**, 115 (2012). https://doi.org/10.1038/nphoton.2011.317
9. X. Zhang, J. Qin, Y. Xue et al., Sci. Rep. **4**, 4596 (2014). https://doi.org/10.1038/srep04596
10. G.H. Munshi, A.M. Ibrahim, L.M. Al-Harbi, Int. J. Photoenergy **2018**, 7 (2018). https://doi.org/10.1155/2018/5094741
11. P. Kaur, S.K. Pandey, S. Kumar et al., Appl. Nanosci. (2015). https://doi.org/10.1007/s13204-014-0394-2
12. H. Khawal, V. Mote, A. Kandasami, B.N. Dole, J. Solid State Electrochem. **22**, 1237 (2017). https://doi.org/10.1007/s10008-017-3833-7
13. G. Voicu, O. Oprea, B. Vasile, E. Andronescu, Dig. J. Nanomater. Biostruct. **8**, 667 (2013)
14. W. Li, G. Wang, C. Chen, J. Liao, Z. Li, Nanomaterials (Basel, Switzerland) **7**, 20 (2017). https://doi.org/10.3390/nano7010020
15. R. Ullah, J. Dutta, J. Hazard. Mater. **156**, 194 (2008). https://doi.org/10.1016/j.jhazmat.2007.12.033
16. J. Singh, A. Rathi, M. Rawat, V. Kumar, K.-H. Kim, Compos. B Eng. **166**, 361 (2019). https://doi.org/10.1016/j.compositesb.2018.12.006
17. H. Khawal, N.D. Raskar, B. Dole, AIP Conf. Proc. **1832**, 080064 (2017). https://doi.org/10.1063/1.4980524
18. G. Vijayaprasath, R. Murugan, G. Ravi, T. Mahalingam, Y. Hayakawa, Appl. Surf. Sci. **313**, 870 (2014). https://doi.org/10.1016/j.apsusc.2014.06.093
19. P.B. Taunk, R. Das, D.P. Bisen, R.K. Tamrakar, N. Rathor, Karbala Int. J. Mod. Sci. **1**, 159 (2015). https://doi.org/10.1016/j.kijoms.2015.11.002
20. J.J. Liu, M.-H. Yu, W.L. Zhou, Appl. Phys. Lett. **87**, 172505 (2005). https://doi.org/10.1063/1.2084321
21. D. Yan, J. Cen, W. Zhang, A. Orlov, M. Liu, CrystEngComm **19**, 584 (2017). https://doi.org/10.1039/C6CE02368A
22. F. Zhang, D. Chao, H. Cui, W. Zhang, W. Zhang, Nanomaterials (2015). https://doi.org/10.3390/nano5020885
23. R. Vinod, M.J. Bushiri, P. Sajan, S.R. Achary, V. Muñoz-Sanjosé, Phys. Status Solidi A **211**, 1155 (2014). https://doi.org/10.1002/pssa.201330394
24. G. Haiyong, Y. Fawang, L. Jinmin, Z. Yiping, W. Junxi, J. Phys. D Appl. Phys. **40**, 3654 (2007)

25. S.H. Jeong, G.C. Park, J.H. Choi et al., J. Nanosci. Nanotechnol. **16**, 11272 (2016). https://doi.org/10.1166/jnn.2016.13492

26. V. Strano, R.G. Urso, M. Scuderi et al., J. Phys. Chem. C **118**, 28189 (2014). https://doi.org/10.1021/jp507496a

27. J. Panda, I. Sasmal, T.K. Nath, AIP Adv. **6**, 035118 (2016). https://doi.org/10.1063/1.4944837

28. O.M. Ozkendir, S. Yildirimcan, A. Yuzer, K. Ocakoglu, Prog. Nat. Sci.: Mater. Int. **26**, 347 (2016). https://doi.org/10.1016/j.pnsc.2016.07.004

29. V. Mote, Y. Purushotham, B. Dole, J. Theor. Appl. Phys. (2012). https://doi.org/10.1186/2251-7235-6-6

30. P. Kumar, B.K. Singh, B.N. Pal, P.C. Pandey, Appl. Phys. A **122**, 1 (2016). https://doi.org/10.1007/s00339-016-0265-7

31. H. Ullah, A. Iqbal, M. Zakria, A. Mahmood, Prog. Nat. Sci. Mater. Int. **25**, 131 (2015). https://doi.org/10.1016/j.pnsc.2015.02.003

32. V.D. Mote, Y. Purushotham, B.N. Dole, Cryst. Res. Technol. **46**, 705 (2011). https://doi.org/10.1002/crat.201100107

33. V. Musat, A. Tabacaru, B. Vasile, V.-A. Surdu, RSC Adv. (2014). https://doi.org/10.1039/c4ra10851e

34. D. Ramimoghadam, M.Z.B. Hussein, Y.H. Taufiq-Yap, Chem. Central J. **7**, 136 (2013). https://doi.org/10.1186/1752-153x-7-136

35. R. Manigandan, K. Giribabu, S. Munusamy et al., CrystEngComm **17**, 2886 (2015). https://doi.org/10.1039/C4CE02390K

36. C. Wang, D. Wu, P. Wang, Y. Ao, J. Hou, J. Qian, Appl. Surf. Sci. **325**, 112 (2015). https://doi.org/10.1016/j.apsusc.2014.11.003

37. A. Hezam, K. Namratha, Q.A. Drmosh et al., CrystEngComm **19**, 3299 (2017). https://doi.org/10.1039/C7CE00609H

38. K.R. Sapkota, W. Chen, F.S. Maloney, U. Poudyal, W. Wang, Sci. Rep. **6**, 35036 (2016). https://doi.org/10.1038/srep35036

39. H. Qi, E.R. Glaser, J.D. Caldwell, S.M. Prokes, J. Nanomater. **2012**, 7 (2012). https://doi.org/10.1155/2012/260687

40. L.K. Jangir, Y. Kumari, A. Kumar, M. Kumar, K. Awasthi, Mater. Chem. Front. **1**, 1413 (2017). https://doi.org/10.1039/c7qm00058h

41. K. Gattu, A. Kashale, K. Ghule et al., J. Mater. Sci.: Mater. Electron. **28**, 1 (2017). https://doi.org/10.1007/s10854-017-7156-3

42. H.A. Khawal, U.P. Gawai, K. Asokan, B.N. Dole, RSC Adv. **6**, 49068 (2016). https://doi.org/10.1039/C6RA04803J

43. M.A. Johar, R.A. Afzal, A.A. Alazba, U. Manzoor, Adv. Mater. Sci. Eng. (2015). https://doi.org/10.1155/2015/934587

44. S.M. Shah, H. Naz, R.N. Ali et al., Arab. J. Chem. **10**, 1118 (2017). https://doi.org/10.1016/j.arabjc.2014.10.001

45. G. Kaur, A. Mitra, K.L. Yadav, Prog. Nat. Sci. Mater. Int. **25**, 12 (2015). https://doi.org/10.1016/j.pnsc.2015.01.012

46. C.A. Arguello, D.L. Rousseau, S.P.S. Porto, Phys. Rev. **181**, 1351 (1969). https://doi.org/10.1103/PhysRev.181.1351

47. V. Strelchuk, O. Kolomys, S. Rarata et al., Nanoscale Res. Lett. **12**, 351 (2017). https://doi.org/10.1186/s11671-017-2127-4

48. S.A. Ansari, M.M. Khan, S. Kalathil, A. Nisar, J. Lee, M.H. Cho, Nanoscale **5**, 9238 (2013). https://doi.org/10.1039/C3NR02678G

49. M.L. Aruna Kumari, L. Gomathi Devi, Environ. Sci. Water Res. Technol. **1**, 177 (2015). https://doi.org/10.1039/c4ew00024b

50. M. Ahmad, E. Ahmed, W. Ahmed, A. Elhissi, Z.L. Hong, N.R. Khalid, Ceram. Int. **40**, 10085 (2014). https://doi.org/10.1016/j.ceramint.2014.03.184

51. B.P. Nenavathu, S. Kandula, S. Verma, RSC Adv. **8**, 19659 (2018). https://doi.org/10.1039/C8RA02237B

52. Q. Ma, X. Lv, Y. Wang, J. Chen, Opt. Mater. **60**, 86 (2016). https://doi.org/10.1016/j.optmat.2016.07.014